Journal of Materials Chemistry C

ROYAL SOCIETY OF CHEMISTRY

PAPER

View Article Online
View Journal | View Issue

Cite this: J. Mater. Chem. C, 2023, 11, 11509

Trap-regulated highly efficient mechanoluminescence and persistent mechanoluminescence of $Ca_2MgSi_2O_7:Eu^{2+}$†

Yingjuan Yan,[abc] Shaofan Fang,[b] Yanyan Li,*[a] Yixuan Xu,[a] Yingdan Song,[a] Zhidong Ma,[c] Yaru Shi,[a] Lei Zhao*[a] and Zhaofeng Wang*[bc]

Mechanoluminescent materials have shown promising applications in visualized mechanical sensing, imaging, and real-time monitoring because of unique mechanics-optics conversion. However, most mechanoluminescent materials exhibit weak intensity and transient emitting behavior, which severely hinders practical applications. In this work, trap-controlled mechanoluminescence (ML) under friction or compression was demonstrated in $Ca_2MgSi_2O_7:Eu^{2+}$ when composited with epoxy resin. In addition to green-emitting ML with relatively good cyclic stability, $Ca_2MgSi_2O_7:Eu^{2+}$ exhibited attractive persistent mechanoluminescence (Pers-ML) behavior (*i.e.*, the sample could emit light continuously after removing the applied mechanical stimulus). This is a significant finding to break the restrictions caused by conventional transient ML behavior. By investigating the intrinsic structure, matrix effects and trap evolution, the "deep" traps and "shallow" traps were found to be responsible for the as-observed ML and Pers-ML, respectively. Based on the physical understanding stated above, a trap-regulating strategy by co-doping with Ho^{3+} was developed, which simultaneously enhanced ML and Pers-ML. These developed materials with highly efficient ML and Pers-ML could be promising for mechanics-driven lighting, displaying, imaging, and sensing applications in various fields.

Received 12th June 2023,
Accepted 26th July 2023

DOI: 10.1039/d3tc02030d

rsc.li/materials-c

1. Introduction

"Smart" manufacturing is advancing rapidly and requires smart sensors with higher performance. To meet this challenge, smart sensors that are miniaturized, integrated, simple and low-cost should be developed.[1–10] Mechanoluminescence (ML) is a fascinating phenomenon in which materials can produce light if subjected to mechanical stimuli, such as fracture, friction, compression, grinding, or stretching.[11–14] With their unique ability to directly convert mechanical energy into light energy, mechanoluminescent materials show widespread applications in stress sensors, smart displays, advanced anti-counterfeiting, crack detectors, and intelligent wearable devices.[15–26] During recent years, increasing numbers of mechanoluminescent materials with excellent performance have been developed, such as ZnS:Cu, ZnS:Mn^{2+},[27] CaZnOS:Mn^{2+},[28] and $SrAl_2O_4:Eu^{2+}$.[29] These mechanoluminescent materials can be used for mechanical sensing to achieve mechanical-distribution imaging and non-destructive stress detection in various fields.[30]

The mechanical-sensing function of mechanoluminescent materials can be realized by establishing a quantitative relationship between the ML intensity and mechanical parameters.[31] Most reported mechanoluminescent materials exhibit transient emitting behaviour under a mechanical stimulus with a short lifetime (10 ns to 10 ms),[32] so mechanical sensing requires capturing and collecting ML signals quickly, which is challenging in practical conditions. Persistent mechanoluminescence (Pers-ML) involves long-lasting luminescence behaviour after a mechanical stimulus. This luminescence phenomenon has a long time of emission and can be detected readily. The detector can capture a luminous signal even in the absence of mechanical stimulation. Few materials that can exhibit Pers-ML have been reported. Smet *et al.* discovered a blue-green mechanoluminescent material, $BaSi_2O_2N_2:Eu^{2+}$, which remains visible for several seconds after removing mechanical stimuli.[33] Yu *et al.* found that $CaAl_2O_4:Eu^{2+}$ exhibited blue Pers-ML, which can be used to detect mechanical information within closed structures.[34] In addition,

[a] School of Physics and Opto-Electronic Technology, Collaborative Innovation Center of Rare-Earth Optical Functional Materials and Devices Development, Baoji University of Arts and Sciences, Baoji, Shaanxi 721016, China. E-mail: shuishouly@126.com, zhaoleibjwl@163.com
[b] Shandong Laboratory of Yantai Advanced Materials and Green Manufacturing, Yantai, Shandong 265503, China
[c] State Key Laboratory of Solid Lubrication, Lanzhou Institute of Chemical Physics, Chinese Academy of Sciences, Lanzhou, Gansu 730000, China. E-mail: zhfwang@licp.cas.cn

† Electronic supplementary information (ESI) available. See DOI: https://doi.org/10.1039/d3tc02030d

previously we reported three types of Pers-ML materials ($Sr_3Al_2O_5Cl_2$:Dy^{3+},[35] $LiGa_5O_8$[36] and $Sr_2P_2O_7$:Eu,Y[22]), among which $Sr_3Al_2O_5Cl_2$:Dy^{3+} could exhibit self-charging Pers-ML behaviour directly under mechanical stimulation without the requirement of pre-irradiation. These long-lifetime mechanoluminescent materials are convenient and practical to use. However, few Pers-ML systems have been reported, and the luminescence intensity is relatively weak and duration is short. Therefore, developing novel Pers-ML materials with higher performance is a rational approach.

Most of the Pers-ML systems reported so far rely on "trap engineering", where electrons in "deep" traps are released into "shallow" traps under mechanical stimulation. Then, the electrons in shallow traps can transfer spontaneously and continuously to luminescent levels under room-temperature thermal disturbance to produce Pers-ML. Persistent luminescence is determined by shallow traps, whereas the ML generation is closely related to deep traps. $Ca_2MgSi_2O_7$:Eu^{2+} (CMSE) has shallow traps with spontaneous emitting behaviours, and deep traps with ML.[37,38] Hence, CMSE meets the prerequisites in terms of trap structure to produce Pers-ML. Herein, we synthesized CMSE and investigated its structure as well as ML and Pers-ML properties. CMSE could exhibit green and reproducible ML with Pers-ML behaviour when composited into epoxy resin. We proposed a trap-engineering strategy by co-doping Ho^{3+} to enhance the ML intensity and Pers-ML performance of CMSE simultaneously. CMSE showed high application value in mechanical reading, imaging, sensing, and monitoring.

2. Experimental

2.1 Synthesis of CMSE powders

$Ca_{2-x}MgSi_2O_7$:xEu^{2+} (x = 0.005, 0.01, 0.03, 0.05, 0.07, 0.09) powders were synthesized by a high-temperature solid-state method. First, stoichiometric amounts of $CaCO_3$ (AR), MgO (AR), SiO_2 (AR), and Eu_2O_3 (99.99%) raw materials were weighed and ground thoroughly in an agate mortar with anhydrous ethanol for 30 min. Then, the mixture was sintered at 1350 °C for 5 h under an atmosphere of 90% N_2 and 10% H_2 in a tube furnace (the function of H_2 was to reduce Eu^{3+} to Eu^{2+}, whereas N_2 was used as a protective gas). After cooling to room temperature, CMSE powders were obtained.

2.2 Fabrication of CMSE-based polymer composites

To analyse ML properties quantitatively, CMSE powders were embedded into transparent polydimethylsiloxane (PDMS) (Sylgard 184; Dow Corning) with a powder-to-polymer mass ratio of 1 : 2. First, 2 g of PDMS base resin and 0.2 g of curing agent at a mass ratio of 10 : 1 was mixed. Then, 1 g of CMSE powder was weighed and dispersed in the mixture stated above by mechanical stirring for 10 min to form a paste that was poured into the mould. Finally, the mould was cured at 80 °C for 60 min, and then CMSE/PDMS composites were obtained.

CMSE powders were also composited into epoxy resin (ER), and the procedure was similar to that of CMSE/PDMS composites (as illustrated in Fig. S1, ESI†). The ratio of CMSE powders to ER and curing agent was 3 : 2 : 1. First, 2 g of epoxy resin and 1 g of curing agent were mixed thoroughly. Then, 3 g of CMSE powders was weighed and stirred for 10 min to disperse in the mixture stated above. Finally, after curing at room temperature for 6 h, CMSE/ER composites were obtained.

2.3 Characterizations

X-ray diffraction (XRD) patterns were recorded by a D2 Phaser (Brucker) in the 2θ range of 10–80° by a step scan mode (step size: 0.02°; count time: 0.1 s per step) equipped with Cu K_α radiation (λ = 1.5418 Å) at 30 kV and 10 mA. Refinement was carried out using the Rietveld method based on the General Structural Analysis System program. Morphology was determined by a scanning electron microscope (VEGA 3 SEM; Tescan). Elemental mappings according to energy-dispersive spectroscopy (EDS) were obtained using a table electron microscope (Ametek Materials Analysis Division). We used a spectrofluorometer equipped with a Xe lamp (FLS980; Edinburgh Instruments) to test the photoluminescence (PL) and photoluminescence excitation (PLE) spectra of samples. Thermoluminescence (TL) spectra were tested with a laser templator (LTTL-3DS; Laser Products Industries). The friction test was conducted using a multi-function friction tester (AS5430, Ningbo Aoshen Technology) equipped with an electrostatic measurement probe (SK050; Keyence). A multi-mode force-induced luminescence detection system (QKLN-ML-2; Qingdao Qingkelangnuo Environmental Protection Technology) was used to characterize the luminescence intensity and ML spectra. This consisted of a stress source (AGS-X 10KN; Shimadzu), a photon-counting module weak-light detector (C13796; Hamamatsu) and a marine optical QE Pro fiber spectrometer (FLAME-S-XP1-ES; White Bear Photonics) with a test wavelength of 300–1100 nm. All optical photographs were taken by a camera (D7500; Nikon) at room temperature.

3. Results and discussion

3.1 Structural analyses

The XRD patterns of as-synthesized $Ca_{2-x}MgSi_2O_7$:xEu^{2+} (x = 0.005, 0.01, 0.03, 0.05, 0.07, and 0.09) powders were investigated (Fig. 1a). All patterns matched well with the standard card of $Ca_2MgSi_2O_7$ (JCPDS card number: 35-0592), and an obvious impurity phase was not observed. Rietveld refinement of CMSE was undertaken to acquire information of crystal structure and local coordination states (Fig. 1b). CMSE was crystallized with the $P\bar{4}2_1m$ (113) space group, and the lattice parameters were $a = b$ = 7.8288(8) Å, c = 5.0052(5) Å, $\alpha = \beta = \gamma$ = 90°, V = 306.77(7) Å^3 and Z = 2, respectively. Experimental results were in good agreement with calculated results. The reliability parameters of Rietveld refinement were R_p = 5.27%, R_{wp} = 6.39% and χ^2 = 1.693, which verified the phase purity of Eu^{2+} doped samples. The crystal structure of CMS is depicted in Fig. 1c; it has a tetragonal melilite-type and non-centrosymmetric crystal structure.[39,40] There are two sites of Ca^{2+}, which are six-coordinated and eight-coordinated, respectively.[41] Comparison

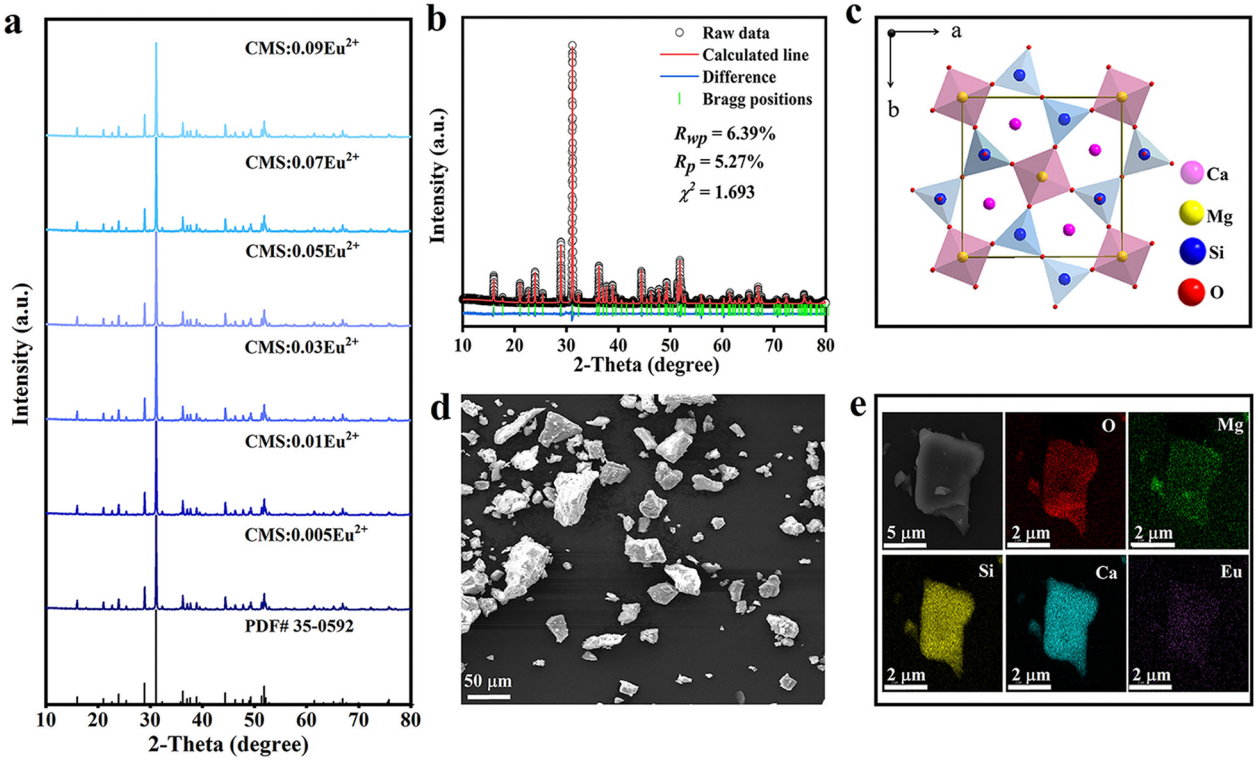

Fig. 1 (a) XRD patterns of a $Ca_{2-x}MgSi_2O_7$:xEu^{2+} (x = 0.005, 0.01, 0.03, 0.05, 0.07, 0.09) series. (b) XRD Rietveld refinement of CMSE. (c) Crystal structure of CMS. (d) SEM image of CMSE particles. (e) Elemental-distribution maps of CMSE based on EDS.

of the ionic radii of Ca^{2+} (CN_6 = 1.00 Å, CN_8 = 1.12 Å), Mg^{2+} (CN_6 = 0.72 Å, CN_8 = 0.89 Å), Si^{2+} (CN_4 = 0.26 Å, CN_6 = 0.40 Å) and Eu^{2+} (CN_6= 1.17 Å, CN_8 = 1.25 Å) suggested that Eu^{2+} should occupy the lattice position of Ca^{2+}. Scanning electron microscope (SEM) was done to reveal the morphology and microstructure of CMSE (Fig. 1d). Samples had an irregular polyhedron morphology of diameter 5–20 μm. Elemental mappings according to EDS confirmed the uniform distribution of Ca, Mg, Si, O, and Eu in particles (Fig. 1e).

3.2 PL, TL, and long persistent luminescence (LPL)

$Ca_2MgSi_2O_7$ could exhibit green PL after doping with Eu^{2+}. Fig. 2a shows the excitation spectrum of CMSE monitored at 536 nm, as well as the emission spectra of $Ca_{2-x}MgSi_2O_7$:xEu^{2+} (x = 0.005, 0.01, 0.03, 0.05, 0.07, and 0.09) excited at 397 nm. The excitation spectrum had peaks of 315 nm, 397 nm, and 460 nm in the range 200–500 nm, which correspond to the $4f^7$–$4f^65d^1$ transition of Eu^{2+}. Meanwhile, under 397 nm excitation, the maximum peak of the emission spectrum located at ~536 nm, which falls in the green-light range and belongs to the typical $4f^65d^1$–$4f^7$ electronic transition of Eu^{2+}.[42–46] The emission spectra revealed that luminescent intensity was strongly dependent on the doping concentration of Eu^{2+} due to concentration quenching, and the optimum Eu^{2+} content was 0.03.

Fig. 2b shows the TL spectra of $Ca_{2-x}MgSi_2O_7$:xEu^{2+} (x = 0.005, 0.01, 0.03, 0.05, 0.07, 0.09) after being simultaneously excited by 254 nm and 365 nm light for 60 s. The TL intensity decreased significantly with an increase in Eu^{2+} content, and the maximum intensity was obtained at an Eu^{2+} content of 0.005. Therefore, we chose CMS:0.005Eu^{2+} for the following trap study. Fig. 2c shows the TL spectrum of CMSE, which contained TL peaks at trap 1 (shallow trap, 353 K) and trap 2 (deep trap, 440 K), respectively.[47] To further explore trap characteristics, we undertook CMSE-charging experiments at different times. As shown in Fig. 2d and Fig. S2a (ESI†), the carrier concentration in the trap saturated when the excitation time reached 20 min. Meanwhile, the TL attenuation curves after 1 min of charging are shown in Fig. 2e and Fig. S2b (ESI†). The TL intensity of trap 1 decreased rapidly within 5 h. After that, most of the carriers in trap 1 could be released. In most cases, TL bands close to the ideal temperature (323–373 K) were suitable for slowly releasing charge carriers at room temperature, which provided a prerequisite for excellent LPL. The fact that the carriers in trap 2 remained basically unchanged provided a possibility for ML generation. Fig. S2c and d (ESI†) show the TL spectra of CMSE after heat treatment at different temperatures for 1 min. As the temperature increased, the carriers in the trap were released gradually due to thermal perturbation, and the TL at low temperature disappeared gradually.[48] Fig. 2f shows the LPL-attenuation curves of CMSE at different temperatures after 1 min of CMSE charging. The initial intensity and decay time of LPL reach their maximum at 353 K because the carrier concentration in the trap was highest at 353 K.[49,50] Fig. S3 (ESI†) shows the long-afterglow attenuation photographs at different temperatures. The initial afterglow intensity was strongest and the afterglow time was longest at

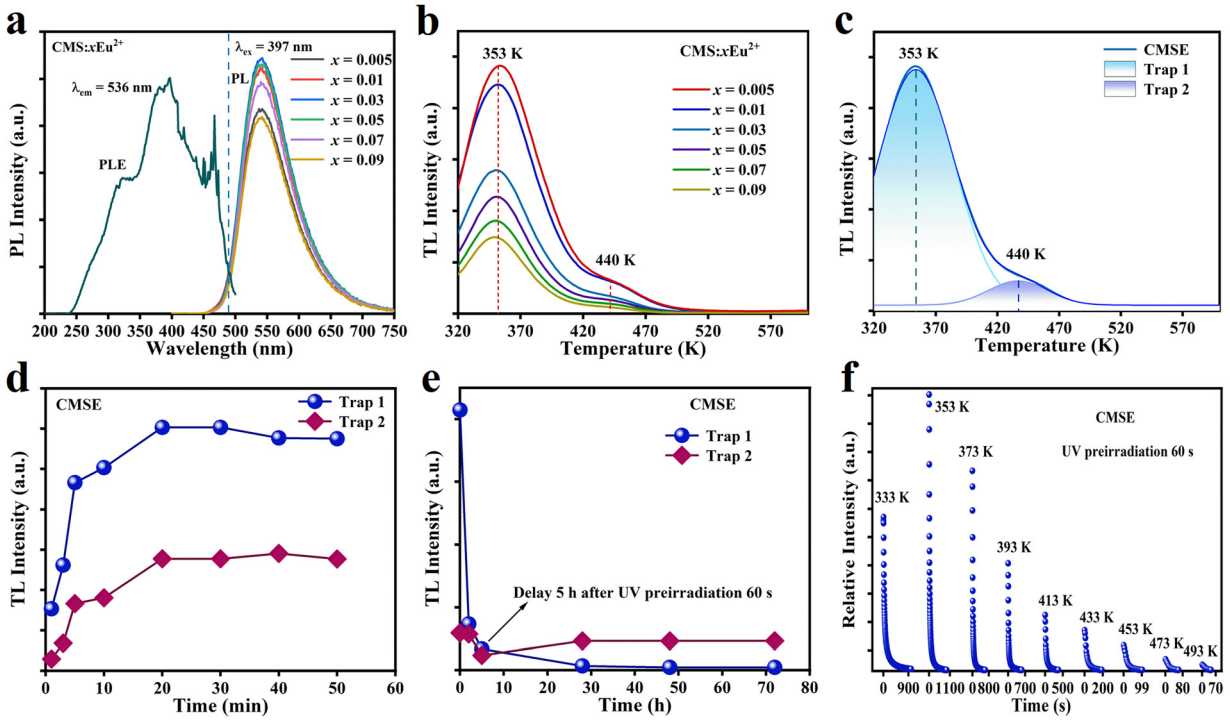

Fig. 2 (a) PLE spectrum of CMSE monitored at 536 nm, and PL spectra of $Ca_{2-x}MgSi_2O_7:xEu^{2+}$ (x = 0.005, 0.01, 0.03, 0.05, 0.07, 0.09) excited by 397 nm; (b) TL spectra of $Ca_{2-x}MgSi_2O_7:xEu^{2+}$ (x = 0.005, 0.01, 0.03, 0.05, 0.07, 0.09) after being simultaneously excited by 254 nm and 365 nm ultraviolet lamps for 60 s; (c) fitted results of the TL spectrum of $Ca_{1.995}MgSi_2O_7:0.005Eu^{2+}$; (d) relationship curves between the intensity of trap 1 and trap 2 and the charging time; (e) intensity variations of trap 1 and trap 2 after 60 s pre-irradiation with the increase of the placing time; (f) LPL decay curves of CMSE at different temperature.

353 K, which agreed with the results in Fig. 2f. Investigation of PL, TL, and LPL properties could provide necessary information on electronic structure and electron transfer of CMSE for further ML study.

3.3 ML, Pers-ML, and underlying mechanisms

To facilitate ML investigations, CMSE powders were composited with PDMS and ER, respectively. When stimulated by stretching, pinching, rubbing, and tearing, CMSE/PDMS samples did not exhibit ML (Fig. 3a). However, CMSE/ER produced bright-green ML under compression or friction stimuli. CMSE particles in flexible PDMS and hard epoxy undergo different interfacial mechanical interactions (*i.e.*, interfacial rubbing in PDMS and compressing in epoxy).[51,52] Hence, the different ML phenomena for CMSE in different matrices suggest that the ML of CMSE should be related to piezoelectricity instead of interfacial friction. Piezoelectric materials such as $Li_{1-x}Na_xNbO_3:Pr^{3+}$,[53] $CaZnOS:Mn^{2+}$,Nd^{3+},[54] $LiNbO_3:Pr^{3+}$,[55] $ZnS:Mn^{2+}$[56] and $LiTaO_3:Bi^{3+}$[57] show similar ML phenomenon. When composited with ER, these materials exhibit ML under compression. These investigations supported our viewpoint in terms of piezoelectricity. Fig. 3b shows the ML spectra of CMSE/ER samples under friction (load: 10 N; rotation speed: 1000 rpm) and the relationship between ML intensity and Eu^{2+} concentration. The ML intensity of CMSE/ER first increased and then decreased with an increase in Eu^{2+} concentration, and the optimum doping concentration of Eu^{2+} was 0.005. This material can be excited by a fluorescent lamp, so all experiments were carried out after exposure to darkness for 5 h to eliminate the influence of afterglow. CMSE/ER also exhibits Pers-ML. As shown in Fig. 3c, when the friction stimulus was removed, CMSE/ER could emit afterglow for ~5 s. Fig. 3d shows the ML curves of CMSE/ER under cyclic compression at 15 mm min^{-1} with a load of 2500 N. The ML intensity of CMSE/ER composite exhibited a slow decay, suggesting its good cycle stability.

To investigate the trap effects on the ML performance of CMSE/ER, we conducted charge–discharge experiments. As shown in Fig. 3e and Fig. S4 (ESI†), the ML intensity of samples increased with an increase in pre-irradiation time until the pre-irradiation time reached >10 min. This observation provided direct evidence that the ML of CMSE/ER was related to the filled carriers in traps. Fig. 3f and Fig. S5 (ESI†) show the ML-intensity variations of CMSE/ER under cyclic compression. Samples were pre-irradiated simultaneously by 254 nm and 365 nm light for 60 s, after which they were placed in the dark for discharging from 0 to 72 h. The ML intensity of CMSE/ER in any cycle decreased rapidly with an increase in discharge time, which demonstrated that the as-observed ML of CMSE in ER originated from trapped carriers. By comprehensively considering the matrix effects and trap effects of the ML performance of CMSE, as well as its intrinsic piezoelectric properties induced by a non-centrosymmetric crystal structure, the ML and Pers-ML processes for CMSE in ER were postulated. First, the applied mechanical stimulation could generate a piezoelectric field

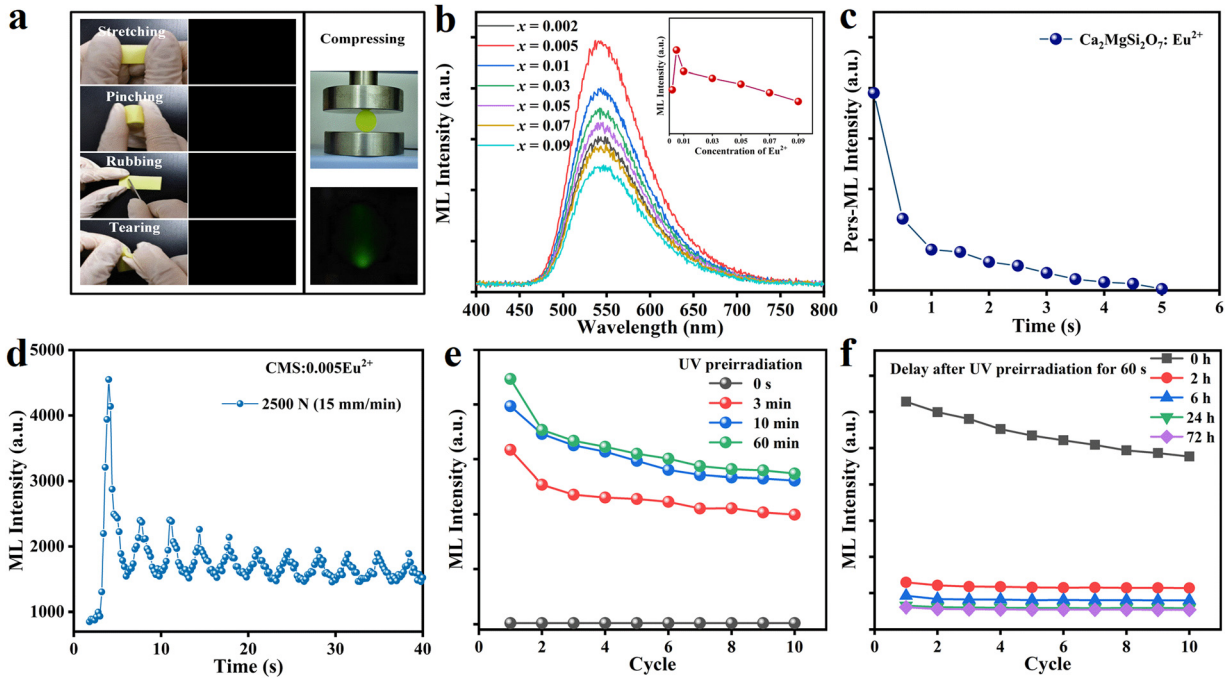

Fig. 3 (a) ML photographs of CMSE/PDMS and CMSE/ER composites under various mechanical stimuli. (b) ML spectra of $Ca_{2-x}MgSi_2O_7$:xEu^{2+} (x = 0.005, 0.01, 0.03, 0.05, 0.07, 0.09) under friction (load: 10 N; rotation speed: 1000 rpm). The inset of (b) depicts ML intensity *vs.* doping concentration of Eu^{2+}. (c) Pers-ML-attenuation curve of CMSE. (d) ML intensity of CMSE/ER under cyclic compression. (e) ML-intensity variations under cyclic compression of samples after pre-irradiation for various times. (f) ML-intensity variations under cyclic compression of samples after placement in the dark for various durations.

inside the material, under which the electrons in deep traps could be released to shallow traps. Then, the electrons in shallow traps could be transferred to the $4f^65d^1$ level of the emission centre of Eu^{2+} through a conduction band. After combining with holes in the ground state, the involved energy of the excited electrons could be released in the form of light to produce the as-observed ML. The shallows traps of CMSE could be activated readily by room temperature (as suggested in Fig. 2e), the electrons released from deep traps to shallow traps could be transferred spontaneously to the excited levels of Eu^{2+} *via* a conduction band. As a result, even though mechanical stimuli had been removed, CMSE could exhibit persistent ML for ~5 s.

3.4 Enhanced performance *via* trap engineering

ML intensity and lasting-time are critical for practical applications. To further enhance ML and Pers-ML performances, Ho^{3+} was introduced in CMSE to control the trap structure through unequal substitution.[58–60] The XRD patterns of $Ca_{1.995-y}MgSi_2O_7$:$0.005Eu^{2+}$,yHo^{3+} (CSMEH, y = 0.003, 0.005, 0.008, 0.01, 0.015) powders are presented in Fig. S6a (ESI†). Significant XRD shifting was not observed with an increase in Ho^{3+}-doping content. This was because in CMSEH, the substitution of Ho^{3+} to Ca^{2+} would arouse lattice shrinkage, whereas the substitution of Eu^{2+} to Ca^{2+} would arouse lattice expansion. Employment of a reduction atmosphere would further produce oxygen vacancies in the structure, which would also arouse lattice shrinkage. These three variations interact with each other, so achieving an obvious and regular change on XRD shifting is difficult. Fig. S6b (ESI†) shows the PL spectra of $Ca_{1.995-y}MgSi_2O_7$:$0.005Eu^{2+}$,yHo^{3+} (y = 0.003, 0.005, 0.008, 0.01, 0.015) excited by 397 nm. Co-doping with Ho^{3+} affected only the PL intensity (variation in peak position was not found), indicating that Ho^{3+} introduced hole traps and served as energy-transport media rather than emission centres in hosts.[58,61] Meanwhile, as the concentration of Ho^{3+} increased, the PL intensity of the sample increased initially and then decreased, with an optimum Ho^{3+}-doping concentration of 0.005. Fig. S6c (ESI†) shows a series of ML spectra of CMSEH/ER under friction (load: 10 N; rotation speed: 1000 rpm). The ML intensity first increased then decreased with increasing Ho^{3+} concentration. When the Ho^{3+} concentration was 0.010, the sample exhibited the best ML performance. The difference in optimal doping concentration between PL and ML was due to their different non-radiative transition pathways. To further investigate the influence of co-doped Ho^{3+} on the trap structure of CMSE, the TL spectra of CMSE and CMSEH after pre-charging for 15 s were obtained (Fig. 4a). After introduction of Ho^{3+}, three TL peaks appeared and the intensity enhanced obviously. These data indicated that the co-doping of Ho^{3+} could improve the trap concentration and introduce additional deep-trap levels, leading to the enhanced ML intensity of CMSEH/ER compared with that of CMSE/ER (load: 10 N; rotation speed: 1000 rpm) (Fig. 4b). Fig. 4c shows the relationship between the applied load and ML intensity of CMSE/ER and CMSEH/ER. Their ML spectra are provided in Fig. S7 (ESI†) with the corresponding ML photographs presented in Fig. 4g. Introduction of Ho^{3+} enhanced the ML intensity and sensitivity of CMSE markedly. Moreover, the

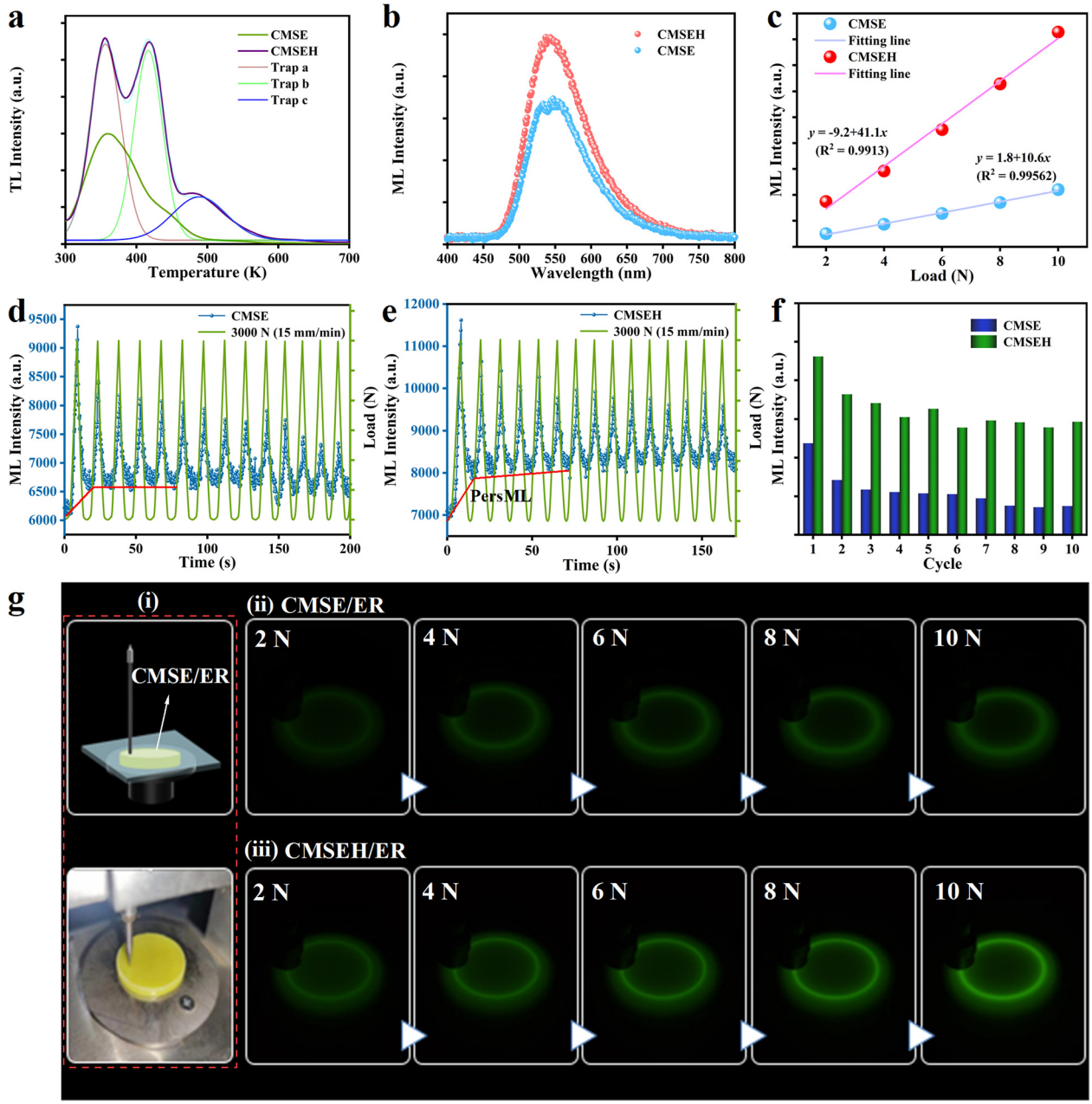

Fig. 4 (a) TL curves of CMSE and CMSEH simultaneously excited by 254 nm and 365 nm UV lamps for 15 s. (b) ML spectra of CMSE/ER and CMSEH/ER under friction (load: 10 N; rotation speed: 1000 rpm). (c) ML-intensity variations of CMSE/ER and CMSEH/ER under various applied loads stimulated by friction. ML-intensity variations of (d) CMSE/ER and (e) CMSEH/ER under cyclic compression, respectively. (f) ML-intensity comparison between CMSE/ER and CMSEH/ER under 10 cyclic compressions. (g)–(i) Schematic diagram and optical photographs of CMSE/ER on a friction-testing machine, and ML photographs of (ii) CMSE/ER and (iii) CMSEH/ER under a load (2 N, 4 N, 6 N, 8 N, or 10 N) stimulated by friction.

ML intensity increased almost linearly with an increase in applied force, suggesting its promise for mechanical sensing. Fig. 4d–f show the ML-intensity variations of CMSE/ER and CMSEH/ER under cyclic compression. The overall ML performance under various mechanical cycles improved. On the one hand, co-doping with Ho^{3+} in CMSE increased lattice asymmetry, which was beneficial for the generation of piezoelectricity. On the other hand, co-doping with Ho^{3+} could regulate the trap structure of CMSE due to unequal substitution (Fig. 4a). Based on these influences, co-doping with Ho^{3+} improved the ML performance of CMSE.

In addition to enhanced ML performance, the increased baseline highlighted by the red lines in Fig. 4d and e suggested that co-doping with Ho^{3+} could also contribute to the Pers-ML performance. Fig. 5a and b show the three-dimensional Pers-ML images of CMSE/ER and CMSEH/ER after 10 s of a friction stimulus (load: 10 N; rotation speed: 1000 rpm), and a direct comparison of decay curves is presented in Fig. 5c. These results confirmed that the introduction of Ho^{3+} in the structure of CMSE could simultaneously enhance the initial Pers-ML intensity and duration (10 s). The optical photographs in Fig. 5d express these

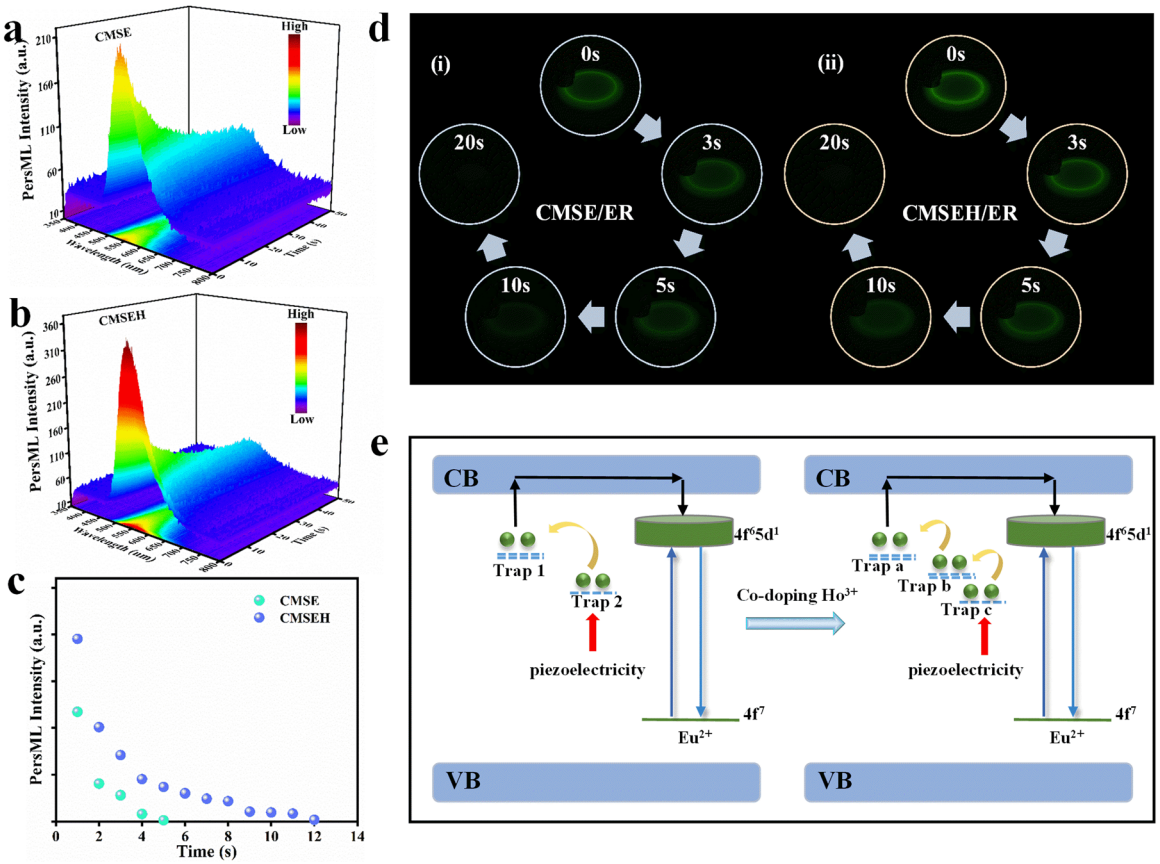

Fig. 5 Three-dimensional Pers-ML images of (a) CMSE/ER and (b) CMSEH/ER. (c) Pers-ML-decay curves of CMSE/ER and CMSEH/ER. (d) Optical photographs of Pers-ML of (i) CMSE/ER and (ii) CMSEH/ER. (e) ML and Pers-ML of CMSE (schematic).

results visually. As discussed in Section 3.3, the ML of CMSE originates from piezoelectric field-assisted de-trapping processes, and Pers-ML is produced by the spontaneous transferring behaviour of the electrons in shallow traps under room-temperature activation. Therefore, the enhanced ML and Pers-ML performance of CMSEH could be ascribed to trap engineering *via* Ho^{3+}, which could improve the trap concentration and introduce additional deep-trap levels (Fig. 4a).

All ML and Pers-ML processes as well as their enhancement mechanisms are illustrated in Fig. 5e. After co-doping with Ho^{3+}, more electrons trapped in deep traps could be stimulated and released to shallow traps. On the one hand, more electrons could be transferred to the excited levels of Eu^{2+} to generate enhanced ML properties. On the other hand, the number of remaining electrons in the shallow traps of CMSEH after removing the mechanical stimulus was larger than that of CMSE. Therefore, after co-doping with Ho^{3+}, more electrons in shallow traps could be transferred spontaneously, thereby leading to enhanced Pers-ML.

4. Conclusions

CMSE powders were synthesized and their optical/luminescent properties investigated comprehensively. When composited with ER, CMSE could exhibit ML and Pers-ML, and could emit green light under (or even after) a mechanical stimulus. The ML of CMSE possessed relatively good cycle stability if subjected to friction. By comprehensively studying the crystal structure, traps and matrix effects, the ML and Pers-ML of CMSE were demonstrated to originate from released carriers in deep traps and shallow traps, respectively. Based on the physical processes stated above, CMSEH was developed to regulate the intrinsic trap structure, which simultaneously enhanced ML and Pers-ML. The developed materials with high ML and Pers-ML performance, as well as an enhancement strategy, could help guide further designs and applications of ML.

Conflicts of interest

There are no conflicts to declare.

Acknowledgements

This work was supported by the Strategic Priority Research Program of the Chinese Academy of Sciences (XDB 0470201), Natural Science Foundation for Distinguished Young Scholars of Gansu Province (20JR5RA572), Special Scientific Research Project of Shaanxi Provincial Department of Education (22JK0245), International Science and Technology Cooperation and Exchanges Project of Shaanxi (2021KW-39), Scientific Research Program

Funded by Shaanxi Provincial Education Department (22JC002), Regional Development Young Scholar Program of the Chinese Academy of Sciences (E30283YRC1), and Baoji University of Arts and Sciences Innovation Research Projects of Postgraduates (YJSCX22YB36).

References

1 T. Lyu, P. Dorenbos, P. Xiong and Z. Wei, *Adv. Funct. Mater.*, 2022, **32**, 2206024.
2 D. Peng, X. Wang, C. Xu, X. Yao, J. Lin and T. Sun, *J. Appl. Phys.*, 2012, **111**, 104111.
3 D. Peng, H. Zou, C. Xu, X. Wang and X. Yao, *J. Alloys Compd.*, 2013, **552**, 463–468.
4 H. Tang, L. Zhao, Z. Liu, Q. Peng, X. Yu, Q. Wang, F. Zhao, M. Deng, Y. Bai, Z. Wang, T. Wang, J. Qiu and X. Xu, *Cell Rep. Phys. Sci.*, 2022, **3**, 101093.
5 Y. Zhao, D. Peng, G. Bai, Y. Huang, S. Xu and J. Hao, *Adv. Funct. Mater.*, 2021, **31**, 2010265.
6 Y. Wen, L. Zhou, Y. Chen, J. Lin, J. Fu, S. Chen, M. Han, J. Li, D. Deng and L. Chen, *Chin. J. Lumin.*, 2022, **43**, 1552–1563.
7 X.-F. Zhao, C.-Z. Hang, H.-L. Lu, K. Xu, H. Zhang, F. Yang, R.-G. Ma, J.-C. Wang and D. W. Zhang, *Nano Energy*, 2020, **68**, 104346.
8 J. Guerrero-Ibanez, S. Zeadally and J. Contreras-Castillo, *Sensors*, 2018, **18**, 1212.
9 X. Gao, F. Zhao, Z. Zhang, Q. Song and M. Song, *Chin. J. Lumin.*, 2022, **43**, 1564–1573.
10 X. Zhou, L. Ning, J. Qiao, Y. Zhao, P. Xiong and Z. Xia, *Nat. Commun.*, 2022, **13**, 7589.
11 C. Wang, H. Hu, D. Zhu and C. Pan, *Sci. Bull.*, 2023, **23**, 559–561.
12 H. Chen, Y. Bai, L. Zheng, L. Wu, L. Wu, Y. Kong, Y. Zhang and J. Xu, *J. Mater. Chem. C*, 2020, **8**, 6587–6594.
13 L. Li, C. Cai, X. Lv, X. Shi, D. Peng, J. Qiu and Y. Yang, *Adv. Funct. Mater.*, 2023, 2301327.
14 C. Wang, H. Hu, D. Zhu and C. Pan, *Sci. Bull.*, 2023, **68**, 559–561.
15 Y. Ding, B. So, J. Cao and L. Wondraczek, *Adv. Sci.*, 2022, **9**, 2201631.
16 Y. Zhuang and R. J. Xie, *Adv. Mater.*, 2021, **33**, 2005925.
17 H. Zhang, D. Peng, W. Wang, L. Dong and C. Pan, *J. Phys. Chem. C*, 2015, **119**, 28136–28142.
18 W. Meng, P. Cai, X. Fu and H. Zhang, *J. Lumin.*, 2022, **248**, 118983.
19 Y. L. Yang, X. C. Yang, J. Y. Yuan, T. Li, Y. T. Fan, L. Wang, Z. Deng, Q. L. Li, D. Y. Wan, J. T. Zhao and Z. J. Zhang, *Adv. Opt. Mater.*, 2021, **9**, 2100668.
20 Z. Ma, J. Zhou, J. Zhang, S. Zeng, H. Zhou, A. T. Smith, W. Wang, L. Sun and Z. Wang, *Mater. Horiz.*, 2019, **6**, 2003–2008.
21 C. Wu, S. Zeng, Z. Wang, F. Wang, H. Zhou, J. Zhang, Z. Ci and L. Sun, *Adv. Funct. Mater.*, 2018, **28**, 1803168.
22 B. Tian, Z. Wang, A. T. Smith, Y. Bai, J. Li, N. Zhang, Z. Xue and L. Sun, *Nano Energy*, 2021, **83**, 105860.
23 C. Chen, Y. Zhuang, X. Li, F. Lin, D. Peng, D. Tu, A. Xie and R. J. Xie, *Adv. Funct. Mater.*, 2021, **31**, 2101567.
24 H. Fang, X. Wang, Q. Li, D. Peng, Q. Yan and C. Pan, *Adv. Energy Mater.*, 2016, **6**, 1600829.
25 C. Wang, Y. Yu, Y. Yuan, C. Ren, Q. Liao, J. Wang, Z. Chai, Q. Li and Z. Li, *Matter*, 2020, **2**, 181–193.
26 X. Zhou, J. Qiao, Y. Zhao, K. Han and Z. Xia, *Sci. China Mater.*, 2022, **65**, 1103–1111.
27 V. K. Chandra, B. P. Chandra and P. Jha, *Appl. Phys. Lett.*, 2013, **103**, 161113.
28 J. C. Zhang, C. N. Xu, S. Kamimura, Y. Terasawa, H. Yamada and X. Wang, *Opt. Express*, 2013, **21**, 12976–12986.
29 Y. Fujio, C.-N. Xu, Y. Terasawa, Y. Sakata, J. Yamabe, N. Ueno, N. Terasaki, A. Yoshida, S. Watanabe and Y. Murakami, *Int. J. Hydrogen Energy*, 2016, **41**, 1333–1340.
30 Y. Z. Ayele, M. Aliyari, D. Griffiths and E. L. Droguett, *Energies*, 2020, **13**, 6250.
31 T. Wang, F. Liu, Z. Wang, J. Zhang, S. Yu, J. Wu, J. Huang, W. Wang and L. Zhao, *Dalton Trans.*, 2022, **51**, 12290–12298.
32 P. Zhang, J. Wu, L. Zhao, Z. Guo, H. Tang, Z. Wang, Z. Liu, W. Chen and X. Xu, *ACS Sustainable Chem. Eng.*, 2023, **11**, 4073–4081.
33 J. Botterman, K. V. d Eeckhout, I. D. Baere, D. Poelman and P. F. Smet, *Acta Mater.*, 2012, **60**, 5494–5500.
34 Y. Cai, S. Liu, L. Zhao, C. Wang, H. Lv, B. Liu, J. Qiu, X. Xu and X. Yu, *J. Adv. Ceram.*, 2022, **11**, 1319–1329.
35 Y. Bai, X. Guo, B. Tian, Y. Liang, D. Peng and Z. Wang, *Adv. Sci.*, 2022, **9**, 2203249.
36 N. Zhang, B. Tian, Z. Wang, A. T. Smith, Z. Ma, Z. Xue and L. Sun, *Adv. Opt. Mater.*, 2021, **9**, 2100137.
37 H. Zhang, H. Yamada, N. Terasaki and C. N. Xu, *J. Electrochem. Soc.*, 2008, **155**, J55–J57.
38 H. Zhang, N. Terasaki, H. Yamada and C.-N. Xu, *Thin Solid Films*, 2009, **518**, 610–613.
39 L. Jiang, C. Chang, D. Mao and C. Feng, *Opt. Mater.*, 2004, **27**, 51–55.
40 I. P. Sahu, D. P. Bisen, K. V. R. Murthy and R. K. Tamrakar, *Luminescence*, 2017, **32**, 1263–1276.
41 H. He, R. Fu, X. Song, R. Li, Z. Pan, X. Zhao, Z. Deng and Y. Cao, *J. Electrochem. Soc.*, 2010, **157**, J69–J97.
42 K. Lyu, E. Song and Z. Xia, *J. Mater. Chem. C*, 2022, **10**, 9636–9643.
43 M. Zhang, Z. Xia and Q. Liu, *J. Mater. Chem. C*, 2017, **5**, 7489–7494.
44 I. P. Sahu, D. P. Bisen and N. Brahme, *Luminescence*, 2015, **30**, 526–532.
45 Q. Lin, T. Gao, Y. Liu, R. Liu, S. Chen, X. Ma and C. Zhao, *J. Rare Earths*, 2022, **41**, 6.
46 Z. Tang, F. Du, Z. Leng, H. Xie, Y. Li and L. Zhao, *J. Rare Earths*, 2022, **22**, 1307.
47 H. Guo, Y. Wang, G. Li, J. Liu and Y. Li, *RSC Adv.*, 2016, **6**, 101731–101736.
48 Y. Fan, X. Jin, M. Wang, Y. Gu, J. Zhou, J. Zhang and Z. Wang, *Chem. Eng. J.*, 2020, **393**, 124799.
49 Z. Liu, L. Zhao, X. Yang, L. Yang, H. Zhang, W. Zeng, X. Yu, J. Qiu and X. Xu, *Chem. Eng. J.*, 2020, **401**, 126119.
50 N. Li, S. Yu, L. Zhao, P. Zhang, Z. Wang, Z. Wei, W. Chen and X. Xu, *Inorg. Chem.*, 2023, **62**, 2024–2032.

51 Z. Ma, Y. Han, Y. Bai, B. Liu and Z. Wang, *Chem. Eng. J.*, 2023, **456**, 141112.
52 H. Zhou, Y. Du, C. Wu, Y. Jiang, F. Wang, J. Zhang and Z. Wang, *J. Lumin.*, 2018, **203**, 683–688.
53 X. Yang, R. Liu, X. Xu, Z. Liu, M. Sun, W. Yan, D. Peng, C. Xu, B. Huang and D. Tu, *Small*, 2021, **17**, 2103441.
54 M. Su, P. Li, S. Zheng, X. Wang, J. Shi, X. Sun and H. Zhang, *J. Lumin.*, 2020, **217**, 116777.
55 D. Tu, C. Xu, A. Yoshida, M. Fujihala, J. Hirotsu and X. Zheng, *Adv. Mater.*, 2017, **29**, 1606914.
56 X. Wang, Q. Guo, H. Zhou, Z. Ma and Z. Wang, *Opt. Mater.*, 2020, **109**, 110289.
57 R. Hu, Y. Zhang, Y. Zhao, X. Wang, G. Li and M. Deng, *Mater. Chem. Front.*, 2021, **18**, 11.
58 C. Wang, Y. Jin, Y. Lv, G. Ju, D. Liu, L. Chen, Z. Li and Y. Hu, *J. Mater. Chem. C*, 2018, **6**, 6058–6067.
59 J. Yuan, Y. Yang, X. Yang, Y. Fan, T. Li, M. Huang, F. Zhang, Q. Li, J. Zhao and Z. Zhang, *J. Mater. Chem. C*, 2021, **9**, 7689–7696.
60 X. Zhou, K. Han, Y. Wang, J. Jin, S. Jiang, Q. Zhang and Z. Xia, *Adv. Mater.*, 2023, **35**, 2212022.
61 M. Pan, Y. Zhong, H. Lin, H. Bao, L. Zheng, R. Hong, B. Dai, D. Yu, D. Zhang and S. Zhuang, *J. Mater. Chem. C*, 2022, **10**, 496–505.